# Centroid depth and mechanism of trench-outer rise earthquakes

Marten Lefeldt[1] and Ingo Grevemeyer[1,2]

[1]*Sonderforschungsbereich 574, Wischhofstr. 1-3, 24148 Kiel, Germany. E-mail: mlefeldt@ifm-geomar.de*
[2]*Leibniz Institut für Meereswissenschaften, IFM-GEOMAR, Wischhofstr. 1-3, 24148 Kiel, Germany*

GJI Seismology

**SUMMARY**
Trench-outer rise earthquakes occur by reactivation or creation of normal faults caused as the oceanic lithosphere approaches a subduction zone and bends into the deep-sea trench. These faults may cut deep enough into the mantle to allow sea water to penetrate into the lithosphere, causing serpentinization. The amount of water carried into the mantle is linked to the maximum depth that the tensional faults cut into the lithosphere, which in turn is directly linked to the maximum focal depths of outer rise normal faulting earthquakes.

We analysed teleseismic $P$ and $S$ waves of seven earthquakes from the trench-outer rise offshore of Central America using teleseismic waveform inversion of broad-band data. For the computation of Green's functions for waveform inversion, probabilistic earthquake locations were calculated. To study the rupture process, earthquake centroid depths and focal mechanisms for a sequence of subevents were calculated. Both, hypocentral depths from the relocation process and the estimated centroid depths from the waveform inversion show that all events occur at shallow depths (<30 km). Furthermore, the locations of the subevents relative to each other suggest that fault planes for $M_w \sim 6$ are in the order of 50 km in length and only 5–10 km in width. Rupture generally propagates downdip and the focal mechanisms change for most events from normal faulting to strike-slip or oblique thrusting with time. The depth at which this mechanism change is observed may represent the depth of the nodal plane between tensional and compressional regions in the incoming plate.

**Key words:** Earthquake source observations; Body waves; Subduction zone processes; Dynamics and mechanics of faulting; Dynamics of lithosphere and mantle; Pacific Ocean.

## 1 INTRODUCTION

Earthquakes in the trench-outer rise of subduction zones are inherently related to plate subduction. Chapple & Forsyth (1979) proposed a model in which outer rise earthquakes are a consequence of plate flexure, while the lithosphere is bent into the trench. Their model suggests that the uppermost lithosphere behaves as a thin elastic plate and that downward flexure at the subduction zone leads to a tensional regime at the top of the plate, grading into a compressional regime at the bottom. Global compilations of earthquake mechanisms based on waveform inversion support this model, as normal faulting events characterize the uppermost 25 km of the incoming lithosphere while thrust faulting and hence compressional fault behaviour occurs at greater depth (e.g. Seno & Gonzalez 1987; Seno & Yamanaka 1996). However, the energy released by great outer rise events, like the 1933 Sanriku $M_s = 8.3$ earthquake, suggest that fracturing took place over almost the entire thickness of the lithosphere, thereby precluding the possibility that such events merely represent a surface tensile crack due to the flexure of the downgoing plate (Kanamori 1971). Such large-scale lithospheric faulting is presumably due to a gravitational pull exerted by the cold sinking lithosphere (Kanamori 1971; Spence 1986).

Multibeam bathymetric coverage of the outer rise region support the view that the oceanic plate may become pervasively fractured prior to subduction (Masson 1991; Kobayashi *et al.* 1998; Ranero *et al.* 2003). At the seafloor, faults have throws of up to 100–500 m and are often 10–50 km long (Kobayashi *et al.* 1998; Ranero *et al.* 2003). Offshore Nicaragua, faulting and fault growth between the outer rise and the trench axis generate a prominent stairway-like seafloor relief prior to subduction. The depth down to which the faults cut into the crust or mantle is poorly known, because the centroid depth of earthquakes is difficult to determine for shallow events in the ocean (e.g. Yoshida *et al.* 1992), though depth phases and waveform modelling suggest that faults may cut often 30–40 km into the mantle (Spence 1986; Tichelaar *et al.* 1992).

Growing evidence suggests that trench-outer rise earthquakes may open pathways for fluids into the crust and mantle that cause extensive hydration of the incoming plate prior to subduction and hence may affect the earth's water cycle. Some of these faults may cut deep enough into the lithosphere (Christensen & Ruff 1988; Hasegawa *et al.* 1994) to reach and react with the lithospheric mantle (Ranero *et al.* 2003), changing 'dry' peridotites to 'wet' serpentinites, which contain up to 13 wt per cent of bound water. In consequence, outer rise processes may affect a number of subduction zone features,

such as the location of the seismogenic coupling zone (Hyndman & Wang 1993), the melt generation under volcanic arcs (Rüpke *et al.* 2002) and Wadati–Benioff earthquakes (Meade & Jeanloz 1991; Kirby *et al.* 1996; Ranero *et al.* 2005).

While trench-outer rise earthquakes for many areas have been studied elsewhere (Chapple & Forsyth 1979; Forsyth 1982; Seno & Gonzalez 1987; Seno & Yamanaka 1996), little is known from earthquakes along the Middle America Trench. In contrast, most recent studies on plate hydration associated with trench-outer rise processes concentrated their efforts on the subduction zone of Costa Rica and Nicaragua (e.g. Ranero *et al.* 2003; Grevemeyer *et al.* 2005, 2007).

In this study we present an investigation of seven outer rise events with $M_w > 5.5$ that occurred between 1992 and 2004 at the Middle America trench. All events have been relocated using traveltime pick data. Centroid depth, focal mechanism, and rupture behaviour were determined from the inversion of body waves using broad-band data. We use these results to show that tensional outer rise events offshore Central America are very shallow with narrow fault plane. We link these results to seismic images published by Ranero *et al.* in the context of mantle hydration.

## 2 TECTONICAL FRAMEWORK AND SETTING

The Middle America Trench (MAT) extends from the Gulf of Tehuantepec to Panama. Earthquakes along the MAT clearly define a Wadati–Benioff zone of landward dipping seismicity where the Cocos plate subducts beneath Central America. The age of the incoming plate (Wilson 1996; Barckhausen *et al.* 2001) increases southwards from 11 to 25 Myr (Fig. 1). The margin normal convergence rate increases from ∼40 to ∼88 mm yr$^{-1}$ from Mexico to southern Costa Rica (DeMets & Dixon 1999). The most prominent features entering the trench are the Tehuantepec fracture zone subducting under southern Mexico and the Cocos Ridge subducting under southern Costa Rica. The crust forming the Cocos plate was created at the fast spreading East Pacific Rise and the Galapagos-Nazca spreading centre. The suture between both domains is located offshore of Nicoya Peninsula (Barckhausen *et al.* 2001). The study area, however, is located to the north of Nicoya Peninsula. Thus, all earthquakes studied here occurred in lithosphere created at the
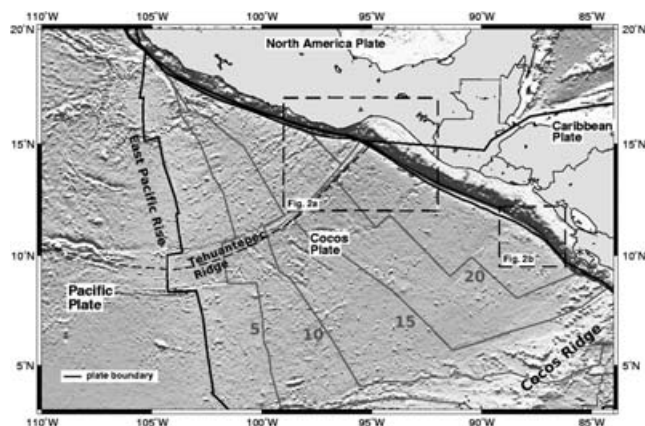


**Figure 1.** Contour map of the Cocos Plate. (Smith & Sandwell 1997) with plate boundaries (modified after Bird 2003). The grey lines denote isochrons with 5 Ma distance (Wilson & Teagle 2002). The dashed frames give the positions of the sections in Fig. 2, the asterix next to the down right corner of the Fig. 2(b) frame shows Nicoya Peninsula.

East Pacific Rise. Offshore of Northern Costa Rica and Nicaragua magnetic anomalies run parallel to the trench axis. To the north of Nicaragua, the trench axis bends and from El Salvador to Mexico magnetic anomalies are subducted at low angle.

High resolution multibeam bathymetry offshore of Nicaragua, El Salvador and Guatemala (Ranero *et al.* 2005) shows that bending-related faulting is pervasive across most of the ocean trench slope (Fig. 2). Multichannel seismic (MCS) reflection data suggested that some of these faults may cut 20 km deep into the lithosphere, which may promote fluid flow down to mantle depth (Ranero *et al.* 2003) and may cause serpentinization of the mantle between the outer rise and the trench axis. Heat flow data obtained on the incoming plate off Nicaragua suggest that bending-related faulting reactivates a vigorous hydrothermal circulation system prior to subduction (Grevemeyer *et al.* 2005) and low seismic velocities occurring where MCS data image deep normal faulting suggest that sea water actually reaches down to mantle depth to cause serpentinization (Grevemeyer *et al.* 2007). Furthermore, seismological data indicates that regional *P* waves from intraslab events at 100–150 km depth show high-frequency late arrivals, most likely trapped in a 2.5–6 km thick low-velocity waveguide at the top of the incoming plate. Such low velocities can best be explained by >5 wt. per cent of water in the subducted crust, which is two to three times the hydration inferred for other slabs (Abers *et al.* 2003).

## 3 DATA

We studied seven trench-outer rise earthquakes that occurred off Central America between 1992 and 2004. Magnitudes range from $M_w = 5.5$ to 6.4 (Table 1). Broad-band data for teleseismic waveform inversion were downloaded at the 'Incorporated Research Institution for Seismology' (IRIS) from IRIS-DMC's archive. Seismograms were chosen from the aspect of good azimuth coverage and good data quality. Here the latter simply means that the data is considered as of good quality if the *P* and *SH* wave is clearly distinguishable from the noise. The records were converted into ground displacement and a three pole low-pass filter (1 Hz) has been applied.

In addition to the waveform data we retrieved phase data from the 'National Earthquake Information Center' (NEIC) of the 'US Geological Survey' (USGS) to relocate the earthquake epicentres. The USGS uses and archives traveltime from a dense worldwide network of stations. However, the distribution of continents and ocean islands leaves a gap over the Pacific Ocean (Fig. 3).

## 4 RELOCATION

Automated teleseismic event locations often come with large uncertainties due to timing errors, phase misslocation (Lomax *et al.* 2000) or limitations of the algorithms, in particular for shallow earthquakes (McGinnis 2001). Earthquake catalogues such as Engdahl & Villaseor (2002) or NEIC/PDE (http://neic.usgs.gov/neis/epic/) have different locations. However, for the following moment tensor inversion, the computation of Green's function is indispensable and sensitive to the epicentre-station distances. Therefore, events were relocated using the NonLinLoc-Package from Lomax *et al.* (2000, 2001) to yield probabilistic event locations. NonLinLoc is a non-linear traveltime calculation code that produces an optimal hypocentre, a misfit function and an estimate of the probability density function from arrival times of seismic phase data using a systematic 3-D grid search.

The phase data together with a 1-D, spherically-layered traveltime grid, which was created for each phase type at each station using
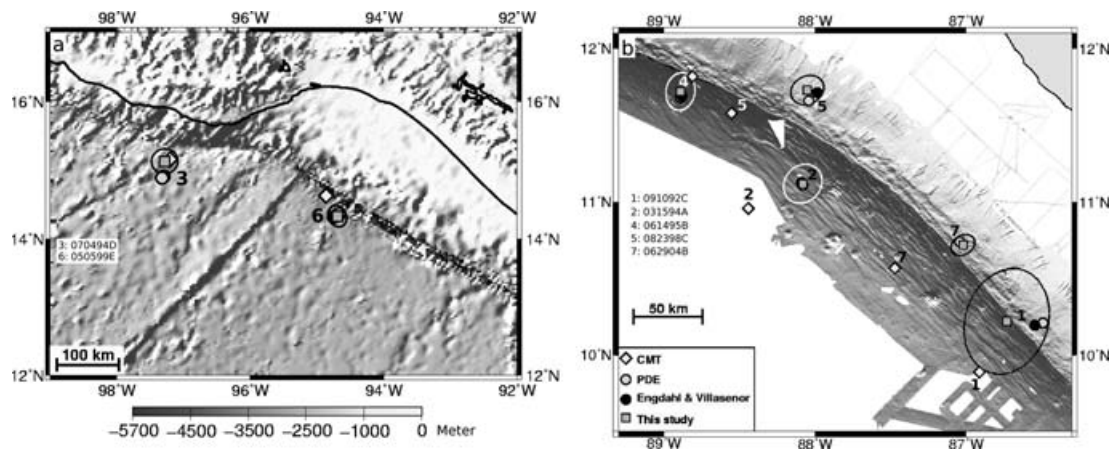
**Figure 2.** Comparison between epicentres from Table 1 and different catalogues. Numbering and labelling is the same as in Table 1. Ellipses are 90 per cent-confidence ellipses. (a) Seafloor topography after Smith & Sandwell (1997). (b) Multibeam bathymetry offshore Nicaragua.

**Table 1.** Events in this study.

| No. | Event | $M$w | Latitude | Longitude | Depth (km) |
|---|---|---|---|---|---|
| 1 | 091092C | 5.9 | 10.22 | −86.73 | 9 |
| 2 | 031594A | 5.8 | 11.12 | −88.08 | 15 |
| 3 | 070494D | 6.4 | 15.13 | −97.28 | 17 |
| 4 | 061495B | 5.5 | 11.72 | −88.89 | 15 |
| 5 | 082398C | 6.7 | 11.73 | −88.05 | 21 |
| 6 | 050599E | 6.1 | 14.33 | −94.69 | 24 |
| 7 | 062904B | 6.3 | 10.72 | −87.02 | 11 |

The labelling (column 2) is the same as used in Harvard CMT Catalogue and simply consists of the date on which the event took place and a letter for what number the event was on that date.

the TauP Toolkit (http://www.seis.sc.edu/software/TauP) with the ak135 1-D TravelTime Tables (Kennett 1995) gave the input for the NonLinLoc-code. The step size of the grid search was 0.05° in latitude and longitude and 2 km in depth. Hypocentre coordinates in Table 1 are results of this calculation. Fig. 2 compares epicentres from different catalogues. The match with acknowledged catalogues, like Engdahl & Villaseor (2002) and NEIC/PDE, is excellent. Epicentres from these catalogues lie throughout into the 90 per cent-confidence ellipse (Fig. 2), which gives the area in which the epicentre is located with a likelihood of 90 per cent.
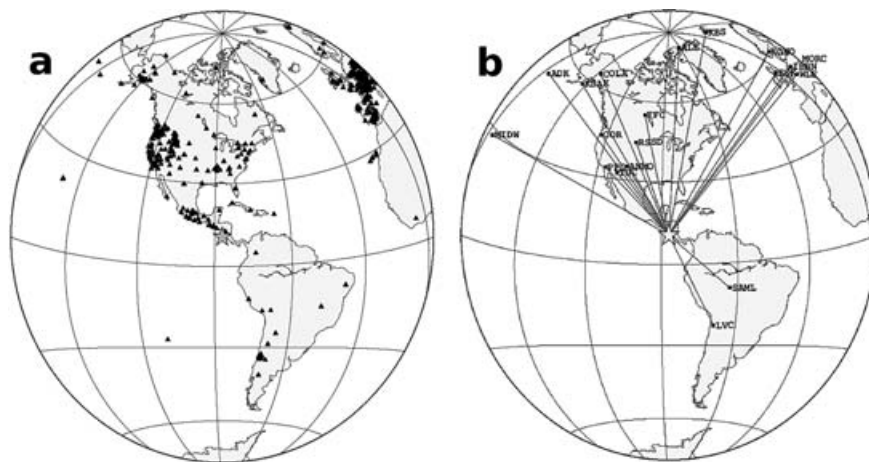
## 5 MOMENT TENSOR INVERSION

To determine focal mechanisms from seismic broad-band data, we used a time-domain iterative inversion method developed by Kikuchi and Kanamori that allows mechanism changes during the rupture sequence. The method is explained in detail elsewhere (Kikuchi & Kanamori 1982, 1986, 1991; Kikuchi & Ishida 1993).

Focal mechanism solutions, like Global CMT or Harvard CMT, are often based on the simplification that a rupture process can be considered as a single point source. This approach allows to determine the overall fault mechanism, but may fail to reveal more complex rupture behaviour. For complex rupture and slip distribution it is more appropriate to describe the source process as a sequence of point sources (subevents), each specified by a moment tensor and its onset time and location (Kikuchi & Kanamori 1991). In this case the overall moment tensor $M$ is a linear combination of—in the most general case 6—elementary moment tensors $M_n$:

$$M = \sum_{n=1}^{N_b} a_n M_n \tag{1}$$

with the coefficients $a_n$.

Let $x_j(t)$ denote the $j$th observed record and $\omega_{jn}(t, p)$ the Green's function due to the $n$th elementary moment tensor $M_n$, where $t$ is

**Figure 3.** Distribution of (a) stations for the relocation process of the 062904B-event (picks from around 450 stations have been used. Data was retrieved from USGS) and (b) of IRIS broad-band seismograph stations used for the waveform inversion of the same event. The star always denotes the epicentre.

**Table 2.** List of station parameters.

| Station | Network | Distance (°) | Azimuth (°) | Phase | Weight |
|---------|---------|--------------|-------------|-------|--------|
| IBBN | GE | 84.5 | 37 | *P* | 1.0 |
| KBS | GE | 81.3 | 11 | *P* | 1.0 |
| MORC | GE | 89.9 | 38 | *P* | 1.0 |
| WLF | GE | 84.0 | 40 | *P* | 1.0 |
| ALE | II | 72.5 | 3 | *P, SH* | 0.8, 0.1 |
| ASCN | II | 74.7 | 101 | *P* | 0.8 |
| ESK | II | 77.8 | 35 | *P* | 1.0 |
| FFC | II | 45.4 | 347 | *P, SH* | 1.0, 0.2 |
| KDAK | II | 68.0 | 328 | *P, SH* | 0.8 |
| PFO | II | 35.3 | 314 | *P, SH* | 1.0, 0.2 |
| ADK | IU | 81.4 | 321 | *P* | 1.0 |
| ANMO | IU | 29.9 | 326 | *P* | 1.0 |
| COLA | IU | 68.2 | 336 | *P, SH* | 1.0, 0.1 |
| COR | IU | 45.9 | 323 | *P, SH* | 1.0, 0.2 |
| KONO | IU | 84.2 | 30 | *P* | 1.0 |
| LVC | IU | 37.6 | 151 | *P, SH* | 1.0, 0.6 |
| MIDW | IU | 85.3 | 297 | *P* | 1.0 |
| RSSD | IU | 36.4 | 339 | *P* | 1.0 |
| SAML | IU | 30.8 | 128 | *P* | 2.5 |
| TRQA | IU | 53.9 | 155 | *P* | 1.0 |
| TUC | IU | 30.7 | 318 | *P, SH* | 1.0, 0.2 |

**Table 3.** Near-source structure.

| $V_p$ (km s$^{-1}$) | $V_s$ (km s$^{-1}$) | $Z$ (km) |
|---------------------|---------------------|----------|
| 1.50 | 0.00 | 3.0 |
| 6.70 | 3.74 | 6.0 |
| 7.20 | 4.10 | 10.0 |
| 8.40 | 4.40 | – |

$V_p$ is the *P* wave and $V_s$ the *SH*-wave velocity, $Z$ the thickness of the layer. The structure is based on results from seismic refraction and wide-angle data (Grevemeyer *et al.* 2007). It should be mentioned here that slide changes of this values don't influence the results of the calculations.

the time and *p* is a parameter that represents both, the onset time $\tau$ and the location of the point source.

May $y_j(t, p)$ represent the synthetic waveform

$$y_j(t, p) = \sum_{n=1}^{N_b} a_n \omega_{jn}(t, p), \tag{2}$$

whereas the coefficients $a_n$ and the parameter $p$ can be obtained from the maximization of the correlation function between the observed and the synthetic waveforms

$$\Psi(p) = \frac{\sum_{j=1}^{N_s} \int [x_j(t) y_j(t, p)] dt}{\sum_{j=1}^{N_s} \int [x_j(t)]^2 dt}, \tag{3}$$

where $N_s$ is the number of used seismograms (Kikuchi & Kanamori 1991). Eq. (3) can be maximized via a grid search over all values of *p*, in which for the computation of overall fault mechanism and depth of a single point source *p* just represents the onset time $\tau$ and the depth *z*. Later, for the calculation of subevents, *p* will contain the locations *l* of the point sources as well.

To demonstrate this inversion procedure we will consider the event 062904B as example, for which we selected 21 vertical components of *P* waveforms and eight horizontal components of *SH* waveforms (Table 2). Fig. 3 shows the distribution of the stations with good signal-to-noise ratio. The coverage is good in the north, but poor in the south, which has been a common problem in this study. Moreover, the number of stations for waveform inversion is much more limited then for the phase data. This has different reasons. First, not all stations listed in the USGS NEIC catalogue operate broad-band sensors. Second, in most seismograms it might indeed be possible to pick first arrivals, but the signal-to-noise ratio might be too poor for waveform modelling. Furthermore, since more stations require more processing time, it is not useful to pick more than a few representative stations out of a 'cluster', like for northwest America or Europe. Further, we applied weight-factors on each station (Table 2) in order to 'down weight' cluster of stations and stations with poor waveform data.

The first step is to determine the representation of the overall fault mechanism in the elementary moment tensors and the depth

of a single point source. Therefore, we computed Green's functions for eight discrete depths of 5–35 km under seafloor with an equal spacing of 5 km beneath the epicentre. We used an increment of 5 km, because, with a sampling interval of 1 s, the minimum depth increment to be resolved by depth phases such as *pP* and *sP* is 2–3 km (Kikuchi & Ishida 1993) and since the coverage of stations shows large gaps, a maximum resolution of 5 km in depth reflects the error of the assessment. The obtained depth might vary from the hypocentre depth, which has been calculated in the relocation process, since the latter only gives the point of the first motion and the former may give the centroid depth of the entire fault motion (Yamanaka & Kikuchi 2003).

The Green's functions were computed using Kikuchi & Kanamori's method (1982, 1991). The near-source structure model used to compute theoretical waveforms is given in Table 3. It is a four-layer structure based on results from seismic refraction and wide-angle data (Grevemeyer *et al.* 2007). Again, the ak135 1-D TravelTime Tables (Kennett *et al.* 1995) have been used as earth model.

Now, the overall fault mechanism is calculated by applying only a single point source together with a broad source time function (Kikuchi & Kanamori 1991), for which we assumed a triangle function with a duration of 15 s. Basically, this method leads to a Centroid Moment Tensor (CMT). These CMTs and the scalar moments, which we obtained with this method are shown in Table 4 for all events. Table 5 gives the corresponding fault mechanisms.

Seismic reflection data and bathymetry image that the bending-related faults dip ~45° trenchwards with a strike of ~120°–130° (Ranero *et al.* 2003), thus a distinction between fault and auxiliary plane could be done (e.g. for the event 062904B we established two solutions, one with a strike of 323° and a dip of 49° and one with a strike of 136° and a dip of 41°. The latter solutions meets the results of Ranero *et al.* suggesting that the former is the auxiliary plane). Thus, the overall mechanisms are similar to the Harvard CMT solution (Table 5). Fig. 4 illustrates the determination of the centroid depth for the event 062904B. The best waveform match was obtained for a depth of 15 km. Table 5 shows these depths for all events.

## 6 SUBEVENTS

As indicated before, the complex rupture of a teleseismic event usually cannot be described by one point source alone, but by a sequence. Each point source is called a subevent.

To identify subevents we used a refined depth grid (Fig. 5) of nine discrete depths with a spacing of 2.5 km and a dip according to Table 4, where the centroid depths from Table 2 represent the central point of the grid. The nine gridpoints had a spacing of 10 km

**Table 4.** Moment tensor for all events.

| Event | Centroid moment tensor ($10^{18}$ N m) | | | | | | $M_0$ ($10^{18}$ N m) |
|---|---|---|---|---|---|---|---|
| | $M_{zz}$ | $M_{xx}$ | $M_{yy}$ | $M_{zx}$ | $M_{zy}$ | $M_{xy}$ | |
| 091092C | $-0.807 \pm 0.033$ | $0.544 \pm 0.021$ | $0.263 \pm 0.018$ | $0.089 \pm 0.210$ | $0.057 \pm 0.137$ | $-0.391 \pm 0.014$ | 0.82 |
| 031594A | $-0.339 \pm 0.017$ | $1.021 \pm 0.016$ | $-0.682 \pm 0.021$ | $-0.302 \pm 0.187$ | $-0.546 \pm 0.120$ | $-0.995 \pm 0.097$ | 1.48 |
| 070494D | $-4.757 \pm 0.021$ | $0.590 \pm 0.024$ | $4.167 \pm 0.017$ | $-1.397 \pm 0.261$ | $0.451 \pm 0.174$ | $-1.920 \pm 0.082$ | 5.10 |
| 061495B | $-6.235 \pm 0.025$ | $2.260 \pm 0.036$ | $3.974 \pm 0.026$ | $1.480 \pm 0.259$ | $-3.152 \pm 0.153$ | $-3.065 \pm 0.051$ | 7.17 |
| 082398C | $-12.078 \pm 0.014$ | $9.701 \pm 0.022$ | $2.378 \pm 0.015$ | $0.758 \pm 0.413$ | $-3.515 \pm 0.227$ | $-5.537 \pm 0.036$ | 12.9 |
| 050599E | $-1.636 \pm 0.019$ | $1.583 \pm 0.017$ | $0.053 \pm 0.010$ | $0.083 \pm 0.174$ | $-0.511 \pm 0.144$ | $-0.555 \pm 0.021$ | 1.78 |
| 062904B | $-3.417 \pm 0.010$ | $1.411 \pm 0.012$ | $2.006 \pm 0.010$ | $0.137 \pm 0.113$ | $-0.536 \pm 0.131$ | $-1.699 \pm 0.007$ | 3.47 |

$M_{xx}$, etc. are defined by Kanamori and Given (1981).

**Table 5.** Centroid depths and fault mechanisms.

| Event | Centroid depth (km) | Our CMT | | | Sum of subevents | | | Harvard CMT | | |
|---|---|---|---|---|---|---|---|---|---|---|
| | | Strike | Dip | Rake | Strike | Dip | Rake | Strike | Dip | Rake |
| 091092C | 30 | 132 | 44 | $-80$ | 126 | 41 | $-89$ | 135 | 24 | $-68$ |
| | | 298 | 47 | $-100$ | 303 | 49 | $-91$ | 292 | 68 | $-99$ |
| 031594A | 15 | 74 | 71 | $-158$ | 64 | 73 | $-148$ | 109 | 46 | $-109$ |
| | | 336 | 69 | $-20$ | 324 | 61 | $-30$ | 316 | 47 | $-71$ |
| 070494D | 25 | 144 | 52 | $-106$ | 139 | 49 | $-98$ | 147 | 45 | $-103$ |
| | | 349 | 41 | $-71$ | 330 | 42 | $-82$ | 345 | 47 | $-78$ |
| 061495B | 10 | 137 | 31 | $-100$ | 134 | 37 | $-110$ | 127 | 34 | $-99$ |
| | | 328 | 59 | $-84$ | 338 | 55 | $-76$ | 318 | 56 | $-84$ |
| 082398C | 20 | 106 | 41 | $-109$ | 111 | 43 | $-100$ | 120 | 45 | $-106$ |
| | | 311 | 52 | $-73$ | 305 | 48 | $-80$ | 322 | 47 | $-74$ |
| 050599E | 15 | 93 | 43 | $-113$ | 121 | 39 | $-102$ | 111 | 49 | $-106$ |
| | | 303 | 51 | $-70$ | 317 | 52 | $-80$ | 313 | 44 | $-73$ |
| 062904B | 15 | 136 | 41 | $-96$ | 133 | 42 | $-99$ | 124 | 52 | $-98$ |
| | | 323 | 49 | $-85$ | 328 | 49 | $-82$ | 317 | 39 | $-80$ |

For each event, the first row gives the fault plane and the second one the auxiliary plane.
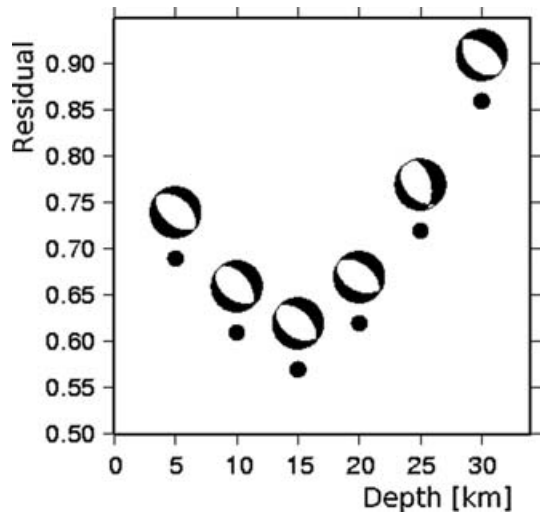


**Figure 4.** Depth-dependency of the residual for a single point source for the 062904B-event and a time window of 40 s starting from the first arrival. A depth of 15 km shows the best waveform-match.

on a line in strike-direction (see Table 4) to determine the subevents locations. This approach is based on the assumption that the entire rupture takes place on a plane which is equal to the CMT fault plane, so that all subevents will take place on a planar fault corresponding to the overall fault mechanism. This limitation is a consequence of the inversion code of Kikuchi and Kanamori, which does not allow a 3-D grid search for subevents (which then could determine the

fault plane). The number of possible solutions would be too large and hence introduce instabilities. Therefore, some additional information about the rupture process are required (Kikuchi & Kanamori 1991).

Now, an iterative procedure is executed, that introduces in every iteration a new subevent with an onset-time $\tau_i$ (time $t$ and $\tau_i$ are discrete values with the increment of the sample rate), represented by a term $\sum a_{ni}\,\omega_{jn}(t, p_i)$, which maximizes the correlation function $\Psi_i$ (eq. 3), where $i$ denotes the $i$th subevent [$i = 1, \dots, N_i$; $N_i =$ Number of subevents (iterations)], so in every new iteration $i$ the observed record $x_j(t)$ in eq. (3) is replaced by a 'new' record

$$x_{ji}(t) = x_j(t) - \sum_{k=1}^{i-1} \sum_{n=1}^{N_b} a_{nk}\,\omega_{jn}(t, p_k), \qquad (4)$$

which then is used as input for the next iteration.

The number of iterations after which a decrease in the residual is not observed determines the number of subevents. Fig. 6 illustrates the procedure for event 062904B. A single event cannot satisfy the observed waveform. The source time function must be very wide to explain the magnitude, which leads to a too wide and prominent first motion. Additionally, later peaks in the observed data cannot be explained. Four iterations are needed to satisfy the records. Additional iterations would not improve the least-square fit. The final results for 062904B are shown in Figs 7 and 8. The comparison of the observed and the synthetic waveforms shows a high degree of concordance (Fig. 7).

The total fault mechanism, which is now the sum of all subevents, changes only slightly (Table 5). The total seismic moment is $M_0 = 3.49 \times 10^{18}$ N m or $M_w = 6.3$, which is consistent with the Harvard
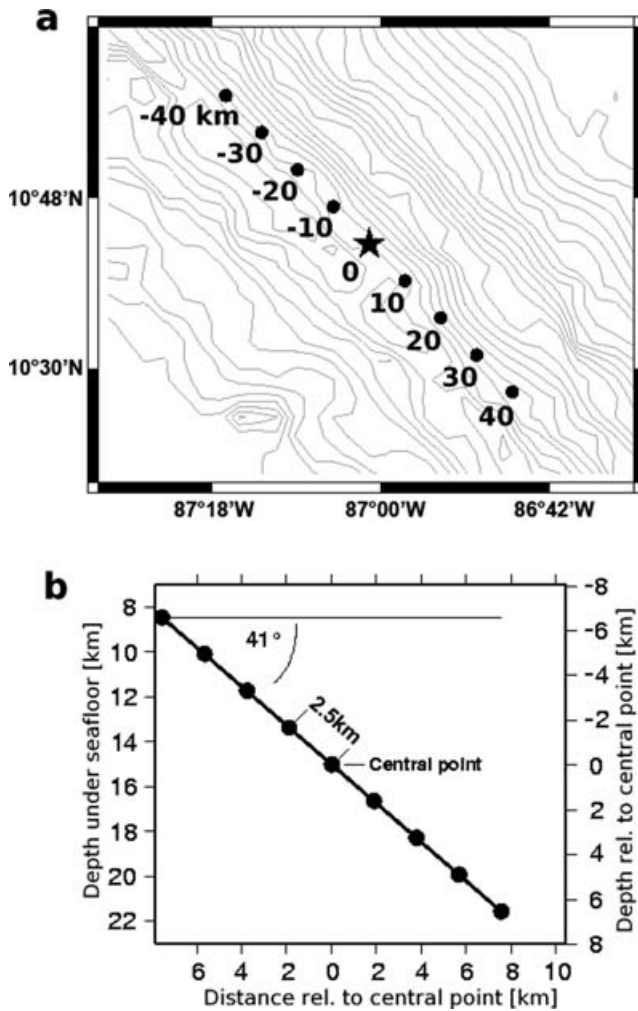
**Figure 5.** Grid scheme for the inversion of the 062904B-earthquake. (a) Nine gridpoints are set up at equal spacing of 10 km on a line (strike of N44°W). The star denotes the epicentre after Table 1. (b) Depth grid.

CMT solution. With time, however, the focal mechanism is changing from normal faulting to strike-slip.

## 7  RELOCATION OF SUBEVENTS

As discussed previously, the inversion code of Kikuchi and Kanamori only allows 2-D grid searches for subevents. To avoid this limitation, we used the NonLinLoc code to recalculate the location of the subevents in a 3-D grid search.

The first arrival observed at station $j$ is associated with the first subevent $i = 1$. It's onset time can be randomly set to $\tau_1 = 0$. Every following subevent $i$ with the onset time $\tau_i$ will occur at the time $(\tau_1 + \tau_{ij}) = \tau_{ij}$ at station $j$, whereas $\tau_{ij}$ most likely will differ from $\tau_i$, since the locations of the point sources are shifting with the rupture process.

Knowledge of the $\tau_{ij}$ for every station $j$ and the azimuths and distances of the stations is already enough to calculate a location relative to the first subevent.

The moment tensor inversion provides us with synthetic waveforms for every station including the first arrival of every considered subevent. Admittedly, these first arrivals are the best-fit result of eq. (3), not the best-fit for every single station.

Instead of maximizing eq. (3), one can also obtain the coefficients $a_n$ and the parameter $p$ from the least-squares criterion

$$\Delta = \sum_{j=1}^{N_s} \int \left[ x_j(t) - \sum_{n=1}^{N_b} a_n \, \omega_{jn}(t, p) \right]^2 \, \mathrm{d}t = \min. \tag{5}$$

As discussed above, a moment tensor solution does not depend on the particular grid, so we can presume that $a_{ni}$ for all subevents are given by the inversion process and now solve eq. (5) independently for every summand

$$\Delta_{ji} = \int \left[ x_j'(t) - \sum_{n=1}^{N_b} a_{ni} \, \omega_{jn}(t, \tau_{ji}) \right]^2 \, \mathrm{d}t. \tag{6}$$

Here $x_j'$ stands for the observed seismogram subtracted by the contributions of subevents $1, \ldots, i - 1$. Note, that the Green's function here is just a function of time $t$ and onset-time $\tau$, since we assumed all source parameters, as source time function, near source structure and source depth to be fixed and the same as in the inversion. Hence, the relocation process here is a relocation of the epicentre only.

Subsequently, we carried out eq. (6) for a range of $\tau_{ji}$, usually starting from $\tau_{ji} = \tau_{ji-1}$ to $\tau_{ji} = \tau_{ji-1} + 2\tau_i$ in steps of 0.5 s. Here, $\tau_{ji-1}$ is the onset time of the previous subevent at station $j$ and $\tau_i$ is the onset time of the subevent under consideration from the inversion process. Then, the lowest value of $\Delta_{ji}$ determines $\tau_{ji}$ for subevent $i$ and station $j$. An example is given in Fig. 9.

This method leads to different onset-times for every station and subevent, which we used as picks to calculate a location relative to the first subevent for every subevent using NonLinLoc. The method is similar to the Master Event Method (e.g. Jackson & Fitch 1979). The results are shown in Fig. 10, the step size for the grid search has been 0.01° in latitude and longitude.

## 8  RESULTS

We relocated hypocentres for seven events from the trench-outer rise offshore of Central America using phase time data (Table 1). Epicentre locations are thorough, error ellipses are small and results from other catalogues mostly lay within these ellipses (Fig. 2). However, the phase time data included only few picks from surface reflections such as $pP$, $sP$, etc., since for shallow, large events recorded at teleseismic distances, it is almost impossible to distinguish between those and direct waves, which limits the depth resolution (e.g. Dziewonski & Anderson 1981). The error margins that we obtained for the hypocentre depths are much higher than those for the epicentre parameters. Statistical errors are usually in the range of $\pm 15$ to $\pm 50$ km. Uncertainties given for the named catalogues are of the same order.

A better method to estimate hypocentre parameters is to find the centroid depth of a point source by moment inversion and waveform modelling. Thus surface reflection are automatically included. The surface reflection of a shallow event arrives shortly after the direct wave. Although its first movement cannot be identified, its contribution to the waveform plays an important role in the inversion process. Fig. 4 illustrates that if one centroid depth minimizes the residual function, a change of $\pm 5$ km for this depth already leads to a significant increase of the residual. In consequence we estimate uncertainties for the centroid depths in Table 5 of $\pm 5$–10 km. However, hypocentre parameters in Table 1 and centroid depths in Table 5 coincide. Note that the hypocentre depth, which gives the location of the initial break and the centroid depth of the entire
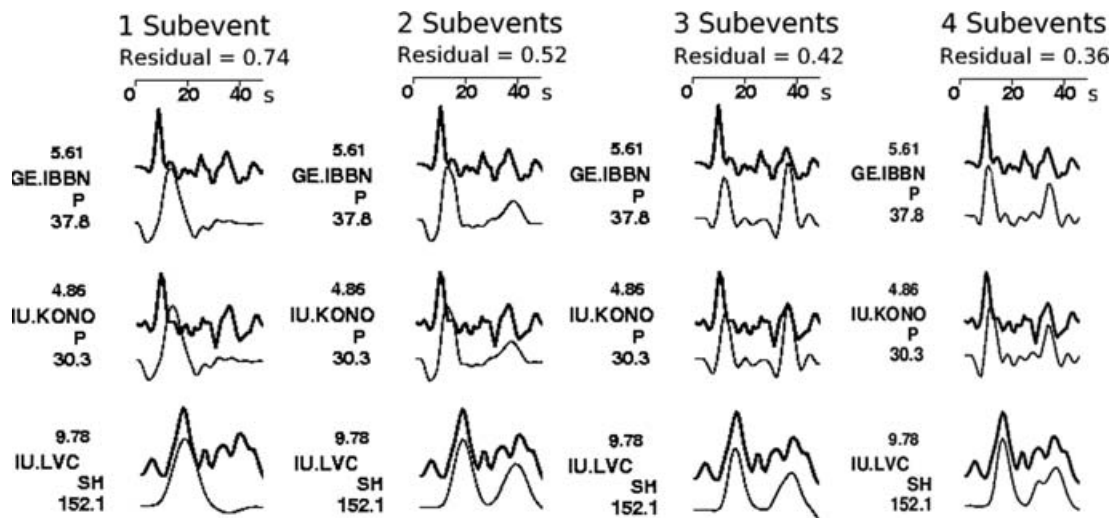
**Figure 6.** Comparison between observed (upper) and synthetic waveforms for different stations and phases. Each column is the result of an inversion process with a different number of iterations (subevents). A further (significant) decrease of the residual cannot be observed after four subevents, which is also sufficient to obtain a good fit (Residual ≤0.4).
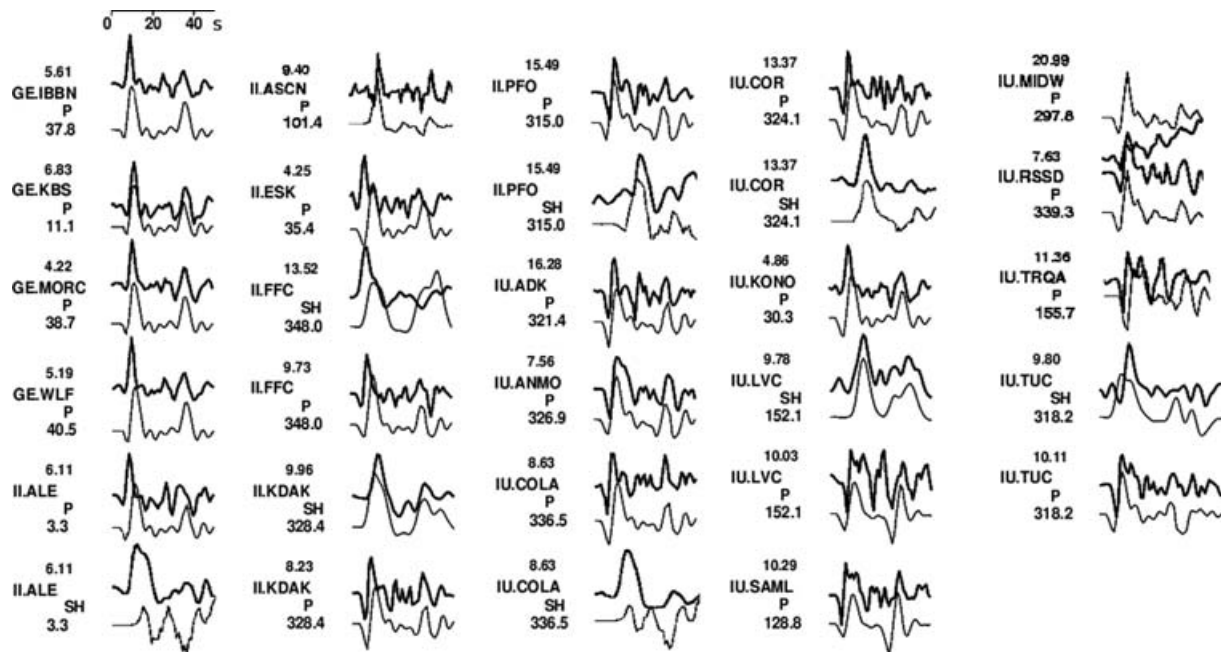


**Figure 7.** Comparison between observed (upper) and synthetic waveforms for all phases used in the 062904B-inversion.

fault motion usually vary from each other. A good agreement between both depths could indicate a fault plane of small extension into depth.

Nevertheless, the calculation of centroid depths via waveform inversion may decrease uncertainties compared to location routines based on traveltime pick, but has its limitations since the calculation of an overall fault mechanism with a single point source cannot reflect the waveform data (normalized residual is usually $\Delta \geqq 0.7$, see Fig. 6) and disregards the details of the waveform.

More confident results are obtained from the determination of subevents. Here we used the depths from Table 4 as centroid points for a finer depth grid with a resolution of 2.5 km. Then, a grid search finds the locations for the subevents that lead to the best match between observed and synthetic waveforms. Assuming that

the depths in Table 5 would be much to shallow, we would find subevents just on the lower gridpoints and we could not obtain a good residual (In general, $\Delta \leq 0.4$ can be considered 'good'). Our results show subevents in the −5.0 to 5.0 km around the centroid depths, even though the depth grid ranges from −10 to 10 km. The normalized residuals are between $\Delta = 0.29$ for event 050599E and $\Delta = 0.44$ for event 091092C for a 50s-cutout counting from the first arrival, whereas the latter is the only one that exceeds $\Delta = 0.4$.

Now, the location of the first subevent in chronological order is conform with the hypocentre, but a limitation of the used moment tensor inversion codes made it necessary to define a 2-D fault plane on which all subevents occur *a priori*. All attempts to use a 3-D grid search led to a non-convergent behaviour and introduced instabilities. In order to deal with this problem we used fault solutions for all
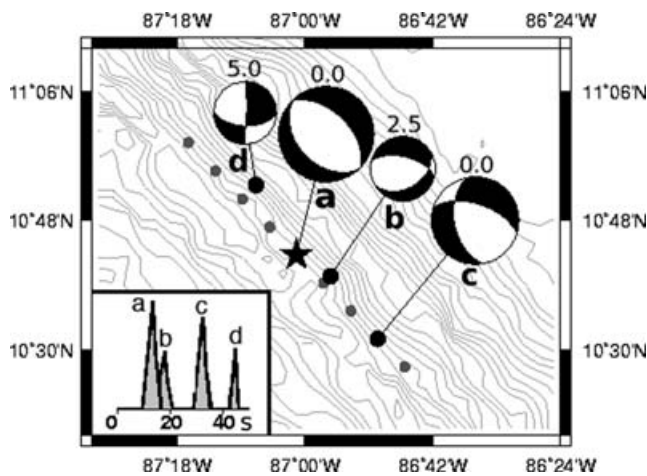
**Figure 8.** Final result of the 062904B-inversion process. The grid scheme is the same as in Fig. 5. The letters beneath the focal mechanism diagram give the chronological order of the onset times of the subevents, the number above gives the depth relative to the centroid depth of 15 km (Table 5). In the down left corner the source time function is shown.

point sources to determine arrival times for each subevent at each station. These arrival times we used to calculate precise locations of the subevents relative to each other.

## 9 DISCUSSION

Teleseismic waveform inversion for earthquakes occurring in the Middle America Trench suffers from a gap in the distribution of stations in the Pacific ocean, and perhaps from the simplification introduced by a 1-D earth model. Nevertheless, we could demonstrate that all events in this area are very shallow and that rupture is propagating downdip in most cases.

It is interesting to note that the rupture sequences of all events but 061495B show a change in mechanism from normal faulting to strike-slip or oblique thrusting. This feature, however, is a robust result and not introduced by the inversion procedure itself. Fig. 11 illustrates the results of a test. The inversion code by Kikuchi and Kanamori allows mechanism changes but also has an option to fix the mechanism. For 062904B, we executed a run with a fixed mechanism for all subevents. The first three subevents we set to the obtained values from section 6 and the fourth and last subevent we set to the overall mechanism from Section 5 {[strike($\Phi$), dip($\delta$), rake($\lambda$)] = (136°, 41°, −96°)}. In both cases the onset-time of the fourth subevent is found to be 41 s after the first arrival. In Fig. 11, we show observed and synthetic waveforms for the subevent, for a strike-slip (left-hand column) and a normal faulting mechanism (right-hand column). As one can see, the introduction of normal faulting leads to a clear difference between observed and synthetic data, while the strike-slip motion improves the fit.

Such a behaviour provides the possibility to estimate the dimension of the fault plane from the distribution of the point sources alone. Usually this is not possible, since a point source only represents the location of an initial break, but tells nothing about how much further the rupture propagates. In the present case five of the seven investigated earthquakes start to rupture downdip as normal faults and end as strike-slip (rupture in strike-direction) or thrust-faults (updip). Therefore, the distance in dip-direction between the shallowest point source and the deepest one gives an estimated for the rupture width. The distance in strike-direction between the two furthermost point sources provides an estimate for the rupture length, only in this case we do not know how much further the rupture continued. In consequence we obtain the minimum rupture length. Via the results from the relocation process for the subevents we find rupture widths of $W = 5–10$ km and minimum rupture lengths of $L_{min} = 25–50$ km. The rupture width seems to be independent of the magnitude. In contrast, the largest event (082398C with $M_w = 6.7$) shows the smallest minimum rupture length ($L_{min} = 25$ km), which might confirm that the actual rupture length is much greater. The subsequent minimum aspect ratios are in the range of $L_{min}/W = 3–10$.
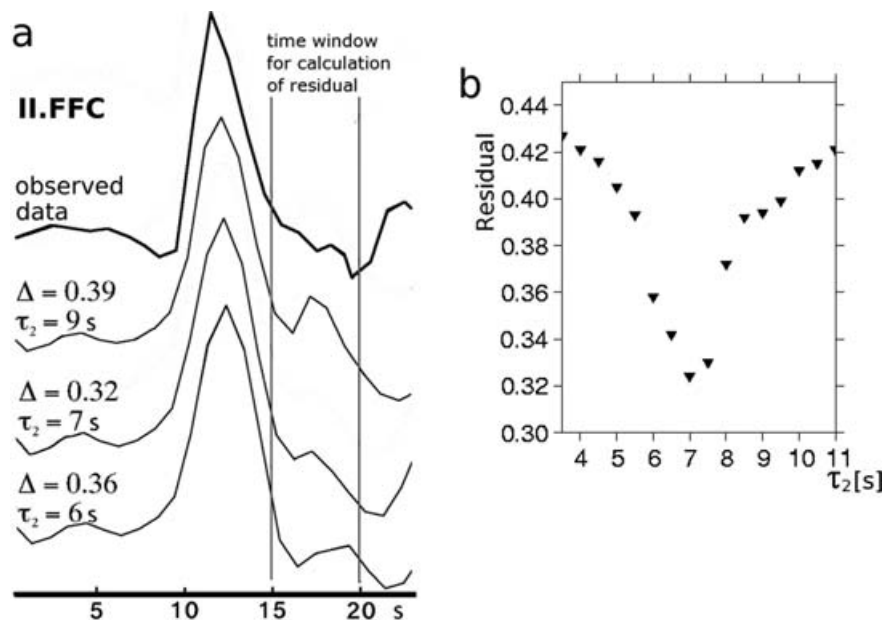


**Figure 9.** (a) Observed seismogram (top) and synthetic waveforms for different onset-times of the second subevent ($\tau_2$). (b) Residual $\Delta$ over onset-time $\tau_2$ for station II.FFC and for the time window showed in (a) with a length of 5 s. The inversion process led to $\tau_2 = 6s$ for this station, the minima obtained here is $\tau_2 = 7s$.
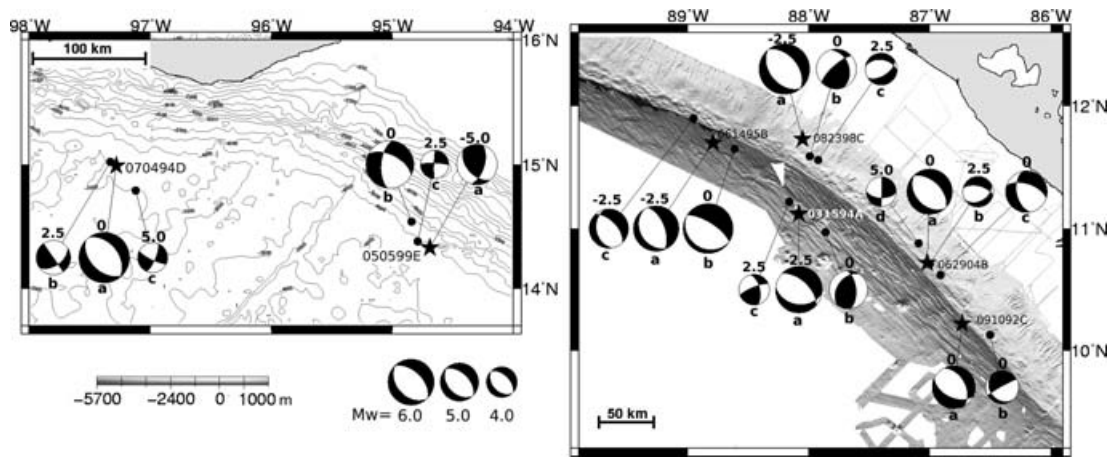
**Figure 10.** Final results of the subevent-relocation process. The stars denote the epicentres of the first subevents, the numbers next to them accord to Table 1. The letters beneath the focal mechanism diagram give the chronological order in which the subevents occurred and the number above gives the depth relative to the first subevent (A negative value means a shallower depth. All depth from moment tensor inversion). Focal mechanism diagrams in one row belong to the same event.

Dowrick & Rhoades (2004) investigated 129 earthquakes from four different regions and found only 17 events with $L/W \geq 10$. The bulk of the data does not exceed $L/W = 6$. Rupture areas are between 40 and 400 km$^2$ for events of magnitudes $M_w = 5.5$–$6.5$. The latter corresponds with our results, but taking into consideration that the



**Figure 11.** Comparison between observed (upper) and synthetic waveforms for two different mechanism for the fourth subevent in the 062904B-event. The left column shows the results of the inversion: a strike-slip subevent can explain the waveform. A neglect of possible changes of the focal mechanism with time and hence the assumption of a normal fault mechanism (consistent with the overall fault mechanism) for the fourth subevent cannot reflect the observed waveforms.

actual aspect ratios for events in this study might be much higher, fault planes of trench-outer rise events offshore Central America seem to be unusually long and narrow.

Accurate centroid depths (Table 5) derived from moment tensor inversion show values between 10 and 25 km below seafloor. (Only for the event 091092C a centroid depth of 30 km was found. However, this event shows also the highest uncertainty and is therefore excluded from the consideration). Combined with the narrow fault planes it follows that large outer rise events offshore Central America are restricted to the upper 15–30 km of the incoming plate.

Seismic images published by Ranero *et al.* (2003) suggest that faults offshore Nicaragua penetrate 10–15 km in to the mantle. Focusing on that area, we can easily estimate the maximum penetration depth into the mantle for those events, which occurred seawards the trench. In that case we only need to subtract the Moho depth of 5–6 km from the entire rupture depth, whereas the latter is given by centroid depths and width of the fault plane. Provided that the centroid depth is located at the upper part of the fault plane (which is unrealistic, since the centroid of the entire fault motion is rather located somewhere in the middle of the fault plane then at its edge), the maximum possible rupture depth can be calculated by adding the width of the fault plane multiplied with the cosine of the dip angle.

Fig. 10 shows that two events (031594A and 061495B) occurred seawards the trench. Those events are also amongst the shallowest (Table 5) with centroid depths of 15 km, respectively, 10 km and dip angles of 46°, respectively, 38°. We did not use the dip angles from the CMT solution in Table 5 for this calculation, since those represent only an average over all dip angles of all subevent. An inversion involving a strong change of focal mechanism as it is the case for the 031594A event cannot provide a realistic overall dip angle. It seems a more appropriate choice to use dip angles of the main shock (the largest subevent) instead. For both events we find rupture plane widths of less than 5 km and in consequence that these rupture penetrate 8–14 km into the mantle. It might therefore be reasonable to hypothesize that seismically imaged faults (Ranero *et al.* 2003) coincide with the rupture plain of large outer rise normal fault events.

As mentioned in the introduction Chapple & Forsyth (1979) proposed a model in which the bending stresses in the incoming plate
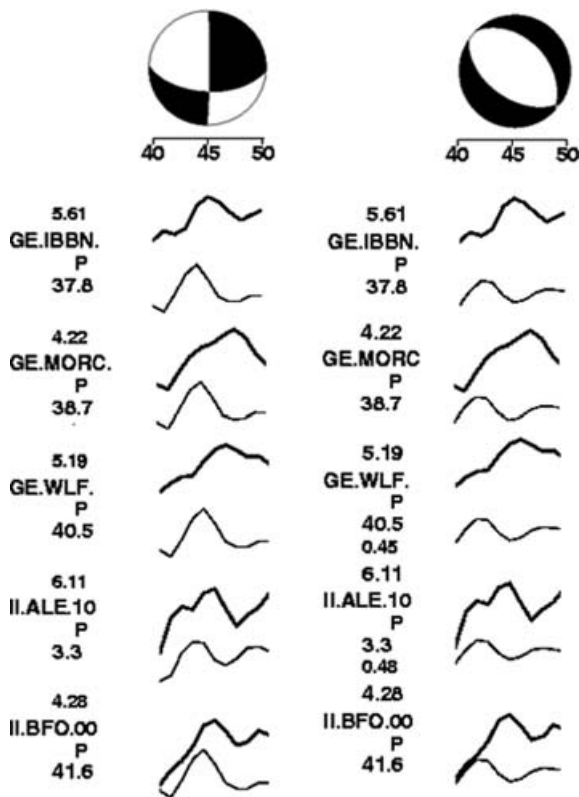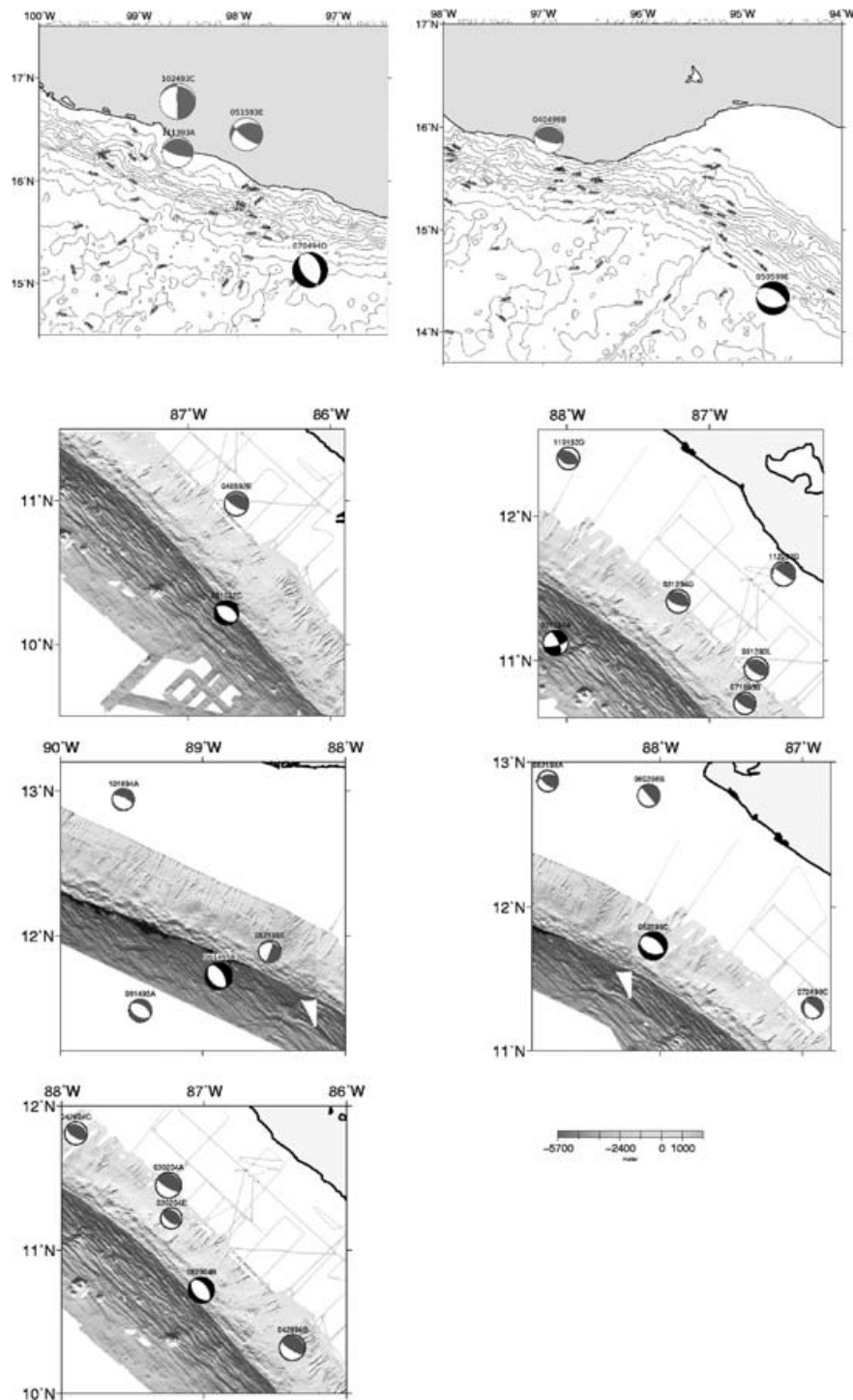
**Figure 12.** Earthquake history for all seven events in this study. Grey focal mechanisms are 'Harvard CMT' solutions for teleseismic events, which occurred before events investigated in this study (black focal mechanisms after Tables 1 and 5).

produce a tensional and a compressional region, both separated by a neutral nodal plane. They found an global average depth for the neutral plane of 30–40 km, whereas their investigation of one thrust event offshore Central America suggests a shallower tensional region. They argued that the lithosphere here is much younger and the plate likely much thinner. The focal depth, which they found for the compressional Middle America event was 19 km. This is in the range of the depth in which our inversions show the reported change

of mechanism. It seems that the focal mechanism changes from normal (tensional) to strike-slip or thrust fault when the rupture front strikes the nodal plane. A large normal fault event that ruptures the surface may provide a pathway for sea water to penetrate the mantle as suggested by Ranero *et al.* (2003), but a compressional regime could present a barrier. In consequence thrust faulting may occur at greater depth than any depth derived for the earthquakes in this study, but those fault may remain dry. Ranero *et al.* (2003) suggested

that the reflectivity of bending-related faults is cause by hydration. Thus, dry compressional faults are perhaps not prominent in seismic reflection data.

Christensen & Ruff (1983, 1988) suggested a model in which the depth of the neutral nodal plane varies both temporally and spatially. They found that after a large underthrusting earthquake the coupling between the incoming and the continental plate can be weakened and tensional stress from slab pull is transferred to the outer rise. In Fig. 12, we plotted events listed in 'Harvard CMT' which occurred before those in our study. All events are thrust fault events with focal depths shallower than 90 km. Most likely they are megathrust or interplate events, since earthquakes due to the dehydration of the incoming plate occur at greater depths (Green & Houston 1995; Kirby *et al.* 1996; Hacker *et al.* 2003). This suggests that all events in this study occur after a partial decoupling of the incoming and the continental plate and therefore are slab pull related. In consequence the depth of the neutral nodal plane found in this study might be greater than it is after the occurrence of a large normal fault outer rise event or before a large thrust event. An interesting question is what would happen to sea water that penetrates during the rupture into a region that is tensional at present, but compressional afterwards. Would it be forced out? However, the good match between our estimation for the depth of the neutral plane and the depth down to which faults are seismically imaged (Ranero *et al.* 2003) suggests that almost the entire tensional regime as we see it during a normal fault rupture is hydrated.

## 10 CONCLUSION

It has been shown that large trench-outer rise earthquakes offshore Central America occur at very shallow depths (<30 km). Strike and dip of these events are consistent with the geometry of the bending-related faults, as it is determined from seismic refraction data and bathymetry. Further, normal fault events at the trench-outer rise seem to occur after large thrust faults events and hence are expected to be related to slab pull.

The rupture processes of normal fault earthquakes is characterized by subevents; a change of the focal mechanism with time from normal fault to strike-slip was observed, provided that the rupture moved unambiguous downdip. This is best explained by a change of the stress field in the lithosphere, which might present the intersection between the upper, tensional and the lower, compressional area. This intersection, which approximately is located ∼8 to 14 km below the Moho, may also present a threshold for sea water to penetrate any deeper. This depth corresponds roughly to the depth of normal faults derived from seismic images (Ranero *et al.* 2003).

This study presents seismological evidence for a hydration of the incoming plate in the Central American Subduction Zone and underlines existing seismic refraction and reflection data. In other subduction zones, where seismic images suggest hydration of the incoming mantle as well, for example, at the North Chile trench (Ranero & Sallares 2004), the presented methods may provide further evidence for mantle hydration in these regions.

## ACKNOWLEDGMENTS

## REFERENCES

Abers, G.A., Plank, T. & Hacker, B.R., 2003. The wet Nicaraguan slab, *Geophys. Res. Lett.*, **30**, doi:10.1029/2002GL015649.

Barckhausen, U., Ranero, C.R., von Huene, R., Cande, S.C. & Roeser, H.A., 2001. Revised tectonic boundaries in the Cocos Plate off Costa Rica: implication for the segmentation of the convergent margin and for plate tectonic models, *J. geophys. Res.*, **109**(B9), 19 207–19 220.

Bird, P., 2003. An updated digital model of plate boundaries, *Geochem. Geophys. Geosyst.*, **4**, 1027, doi:10.1029/2001GC000252.

Chapple, W.M. & Forsyth, D.W., 1979. Earthquakes and bending plates at trenches, *J. geophys. Res.*, **84**, 6729–6749.

Christensen, D.H. & Ruff, L., 1983. Outer-rise earthquakes and seismic coupling, *Geophys. Res. Lett.*, **10**, 697–700.

Christensen, D.H. & Ruff, L., 1988. Seismic coupling and outer rise earthquakes, *J. geophys. Res.*, **93**, 13421–13444.

DeMets, C. & Dixon, T.H., 1999. New kinematic models for Pacific-North America motion from 3 Ma to present, I: evidence for steady motion and biases in the NUVEL-1A model, *Geophys. Res. Lett.*, **26**, 1921–1924.

Dowrick, D.J. & Rhoades, D.A., 2004. Relations between earthquake magnitude and fault rupture dimensions: how regionally variable are they? *Bull. seism. Soc. Am.*, **94**, 776–788.

Dziewonski, A.M. & Anderson, D.L., 1981. Preliminary reference Earth model, *Phys. Earth planet. Int.*, **25**, S297–356.

Engdahl, E.R. & Villaseor, A., 2002. Global seismicity: 1900–1999, in Lee, W.H.K., Kanamori, H., Jennings, P.C. & Kisslinger, C., eds, *International Handbook of Earthquake and Engineering Seismology,* Part A, Chapter 41, pp. 666–690, Academic Press, London.

Forsyth, D.W., 1982. Determinations of focal depths of earthquakes associated bending of oceanic plates at trenches, *Phys. Earth planet. Int.,* **28**, 141–160.

Green, H.W. & Houston, H., 1995. The mechanics of deep earthquakes, *Ann. Rev. Earth Planet. Sci.,* **23**, 169–213.

Grevemeyer, I., Kaul, N., Diaz-Naveas, J.L., Villinger, H., Ranero, C.R. & Reichert, C., 2005. Heat flow and bending-related faulting at subduction trenches: case studies offshore of Nicaragua and Central Chile, *Earth planet. Sci. Lett.,* **236**, 238–248.

Grevemeyer, I., Ranero, C.R., Flueh, E.R., Klaeschen, D. & Bialas, J., 2007. Passive and active seismological study of bending-related faulting and mantle serpentinization at the Middle America trench, *Earth planet. Sci. Lett.,* **258**, 528–542.

Hacker, B.R., Peacock, S.M., Abers, G.A. & Holloway, S.D., 2003. Subduction factory 2. Are intermediate-depth earthquakes in subducting slabs linked to metamorphic dehydration reactions? *J. geophys. Res.,* **108**, doi:2010.1029/2001JB001129.

Hasegawa, A., Horiuchi, S. & Umino, N., 1994. Seismic structureof the northeastern Japan convergent margin: a synthesis, *J. geophys. Res.,* **99**, 22 295–22 311.

Hyndman, R.D. & Wang, K., 1993. Thermal constraints on the zone of major thrust earthquake failure: the Cascadia subduction zone, *J. geophys. Res.,* **98**, 2039–2060.

Jackson, J. & Fitch, T., 1979. Seismotectonic implication of the relocation aftershock sequences in Iran and Turkey: an application of the master event technique, *Geophys. J. R. astr. Soc.*, **57**, 209–229.

Kanamori, H., 1971. Seismological evidence for lithospheric normal faulting: the Sanriku earthquake of 1933, *Phys. Earth planet. Inter.*, **4**, 289–300.

Kanamori, H. & Given, J.W., 1981. Uses of Long-Period Surface Waves for Rapid Determination of Earthquake Source Parameters, *Phys. Earth Planet. Int.,* **27**, 8–31.

Kennett, B.L.N, Engdahl, E.R. & Buland, R., 1995. Constraints on seismic velocities in the Earth from travel times, *Geophys. J. Int.*, **122,** 108–124.

Kikuchi, M. & Kanamori, H., 1982. Inversion of complex body waves, *Bull. seism. Soc. Am.*, **72,** 491–506.

Kikuchi, M. & Kanamori, H., 1986. Inversion of complex body waves II, *Phys. Earth planet. Int.*, **43,** 205–222.

Kikuchi, M. & Kanamori, H., 1991. Inversion of complex body waves III, *Bull. seism. Soc. Am.*, **81,** 2335–2350.

Kikuchi, M. & Ishida, M., 1993. Souce retrieval for deep local earthquakes with broadband records, *Bull. seism. Soc. Am.*, **83,** 1855–1870.

Kirby, S.H., Engdahl, E.R. & Denlinger, R., 1996. Intraslab earthquakes and arc volcanism: dual physical expressions of crustal and uppermost mantle metamorphism in subducting slabs, in *Subduction: Top to Bottom*, Vol. 96, pp. 195–214, eds Bebout, G.E. *et al.* Geophysical Monograph, Washington D.C., American Geophysical Union.

Kobayashi, K., Nakanishi, M., Tamaki, K. & Ogawa, Y., 1998. Outer slope faulting associated with western Kuril and Japan trenches, *Geophys. J. Int.*, **134,** 356–372.

Lomax, A., Virieux, J., Volant, P. & Berge, C., 2000. Probabilistic earthquake location in 3D and layered models: introduction of a Metropolis-Gibbs method and comparison with linear locations, in *Advances in Seismic Event Location*, pp. 101–134, eds Thurber, C.H. & Rabinowitz, N., Kluwer, Amsterdam.

Lomax, A., Zollo, A., Capuano, P. & Virieux, J., 2001. Precise, absolute earthquake location under Somma-Vesuvius volcano using a new 3D velocity model, *Geophys. J. Int.*, **146,** 313–331.

Masson, D.G., 1991. Fault patterns at outer trench walls, *Mar. geophys. Res.,* **13,** 209–225.

Meade, C. & Jeanloz, R., 1991. Deep focused earthquakes and recycling of water into the Earth s mantle, *Science*, **252,** 68–72.

McGinnis, S., 2001. On the effects of geometry in discrete element numerical earthquake simulations, *PhD thesis*, University of Colorado.

Ranero, C.R. & Sallares, V., 2004. Geophysical evidence for hydration of the crust and mantle Nazca plate during bending at the north Chile trench, *Geology*, **32,** 549.

Ranero, C.R., Phipps Morgan, J., McIntosh, K. & Reichert, C., 2003. Bending, faulting, and mantle serpentinization at the Middle America Trench, *Nature*, **425,** 367–373.

Ranero, C.R., Villaseor, A., Phipps Morgan, J. & Weinrebe, W., 2005. Relationship between bendfaulting at trenches and intraslab seismicity, *Geosys., Geophys., Geochem.,* **6,** doi:10.1029/2005GC000997.

Rüpke, L., Phipps Morgan, J., Hort, M. & Connolly, J.D.A., 2002. Are the regional variations in Central America arc lavas due to differing basaltic peridotitic slab sources of fluids? *Geology*, **30,** 1035–1038.

Seno, T. & Gonzalez, D.G., 1987. Faulting caused by earthquakes beneath the outer slope of the Japan Trench, *J. Phys. Earth*, **35,** 381–407.

Seno, T. & Yamanaka, Y., 1996. Double seismic zones, compressional deep trench-outer rise events and superplumes, in *Subduction: Top to Bottom*, Vol. 96, pp. 347–355, eds Bebout, G.E., Scholl, D.W., Kirby, S.H. & Platt, J.P., Geophys. Monogr, AGU, Washington, DC.

Smith, W.H.F. & Sandwell, D.T., 1997. Global seafloor topography from satellite altimetry and ship depth soundings, *Science*, **277,** 1957–1962.

Spence, W., 1986. The 1977 Sumba earthquake series: evidence for slab pull force acting at a subduction zone, *J. geophys. Res.*, **91,** 7225–7239.

Tichelaar, B.W., Christensen, D.H. & Ruff, L.J., 1992. Depth extent of rupture of the 1981 Chilean Outer-rise earthquake as inferred from long-period body waves, *Bull. seism. Soc. Am.*, **82,** 1236–1252.

Wilson, D.S., 1996. Fastest known spreading on the Miocene Cocos-Pacific Plate boundary, *Geophys. Res. Lett.*, **23,** 3003–3006.

Wilson, D.S., Teagle, D.A.H. & Acton, G.D. *et al.*, 2003. Proc. ODP, Init. Repts., 206 [WWW document] URL http://www-odp.tamu.edu/publications/206_IR/206ir.htm

Yamanaka, Y. & Kikuchi, M., 2003. Source processes of the recurrent Tokachi-oki earthquake on September 26, 2003, inferred from teleseismic body waves, *Earth Planet. Sci.*, **55,** e21–e24.

Yoshida, Y., Satake, K. & Abe, K., 1992. The large normal-faulting Mariana earthquake of April 5, 1990 in uncoupled subduction zone, *Geophys. Res. Lett.*, **19,** 297–300.